arXiv:1701.00308v1 [astro-ph.SR] 2 Jan 2017

"Dandelion" Filament Eruption and Coronal Waves Associated with a Solar Flare on 2011 February 16

Denis P. Cabezas[1,2,3], Lurdes M. Martínez[2], Yovanny J. Buleje[2], Mutsumi Ishitsuka[1], José K. Ishitsuka[1], Satoshi Morita[4], Ayumi Asai[5], Satoru UeNo[3], Takako T. Ishii[3], Reizaburo Kitai[3,6], Shinsuke Takasao[3], Yusuke Yoshinaga[3,7], Kenichi Otsuji[3,4], and Kazunari Shibata[3]

denis@kwasan.kyoto-u.ac.jp

Received _____; accepted _____

[1]Geophysical Institute of Peru, Calle Badajoz 169, Mayorazgo IV Etapa, Ate Vitarte, Lima, Peru

[2]Centro de Investigación del Estudio de la Actividad Solar y sus Efectos Sobre la Tierra, Facultad de Ciencias, Universidad Nacional San Luis Gonzaga de Ica, Av. Los Maestros S/N, Ica, Peru

[3]Kwasan and Hida Observatories, Kyoto University, Yamashina, Kyoto, 607-8471, Japan

[4]National Astronomical Observatory of Japan, Osawa, Mitaka, Tokyo 181-8588, Japan

[5]Unit of Synergetic Studies for Space, Kyoto University, Sakyo, Kyoto, 606-8502, Japan

[6]Bukkyo University, Kita, Kyoto, 603-8301, Japan

[7]Department of Astronomy, Kyoto University, Sakyo, Kyoto 606-8502, Japan

ABSTRACT

Coronal disturbances associated with solar flares, such as Hα Moreton waves, X-ray waves, and extreme ultraviolet (EUV) coronal waves are discussed herein in relation to magnetohydrodynamics fast-mode waves or shocks in the corona. To understand the mechanism of coronal disturbances, full-disk solar observations with high spatial and temporal resolution over multiple wavelengths are of crucial importance. We observed a filament eruption, whose shape is like a "dandelion", associated with the M1.6 flare that occurred on 2011 February 16 in the Hα images taken by the Flare Monitoring Telescope at Ica University, Peru. We derive the three-dimensional velocity field of the erupting filament. We also identify winking filaments that are located far from the flare site in the Hα images, whereas no Moreton wave is observed. By comparing the temporal evolution of the winking filaments with those of the coronal wave seen in the extreme ultraviolet images data taken by the Atmospheric Imaging Assembly on board the *Solar Dynamics Observatory* and by the Extreme Ultraviolet Imager on board the *Solar Terrestrial Relations Observatory-Ahead*, we confirm that the winking filaments were activated by the EUV coronal wave.

Subject headings: Sun: chromosphere — Sun: corona — Sun: filaments — Sun: flares — Sun: magnetic fields — shock waves

1. Introduction

Coronal disturbances associated with solar flares have been discussed in relation to magnetohydrodynamics (MHD) fast-mode waves or shocks in the corona (Patsourakos & Vourlidas 2012; Warmuth 2015, and references therein). Moreton waves are flare-associated propagating wavelike features seen in Hα, especially in its wings (Moreton 1960; Moreton & Ramsey 1960; Athay & Moreton 1961). This dynamic phenomenon is directional in restricted solid angles with arc-like fronts, and propagates away from the flare site at speeds of the order of 500 – 1500 km s^{-1}. Uchida (1968) proposed the following mechanism for producing Moreton waves: they are the intersection of MHD fast-mode shocks propagating in the corona with chromospheric plasma. A good correlation between Hα Moreton wave and Type-II radio bursts (Kai 1970) also supports this scenario.

Extreme ultraviolet (EUV) coronal waves are wavelike disturbances or expanding-dome structures observed in EUV passbands in the solar corona associated with flares. They were first observed by the Extreme-ultraviolet Imaging Telescope (EIT; Delaboudinière et al. 1995) on board the *Solar and Heliospheric Observatory* (*SOHO*; Domingo et al. 1995) and were called EIT waves (Thompson et al. 1999; Thompson 2000). Although EIT waves were expected to be the coronal counterpart of Moreton waves, the propagating speed was much lower (170 – 350 km s^{-1}) than that of Moreton waves (Klassen et al. 2000; Thompson & Myers 2009). Therefore, the nature of EIT waves was questioned due the discrepancies on their physical characteristics as compared to Moreton waves. Simultaneous observations of EIT waves and Hα Moreton waves (Eto et al. 2002) show that EIT wavefronts are not co-spatial with those of Moreton waves. On the other hand, Warmuth et al. (2004a,b) and Vršnak et al. (2016) discuss that the velocity discrepancy can be explained by the deceleration of coronal waves.

"Fast" EUV waves associated with flares have been observed by recent EUV

observations made mainly by the Atmospheric Imaging Assembly (AIA; Lemen et al. 2012) on board the *Solar Dynamics Observatory* (*SDO*; Pesnell, et al. 2012) and by the Extreme-Ultraviolet Imager (EUVI) from the Sun-Earth Connection Corona and Heliospheric Investigation (SECCHI; Howard et al. 2008) on board the *Solar Terrestrial Relations Observatory* (*STEREO*; Kaiser et al. 2008). Since the speed of the wavelike features is sometimes very fast and comparable to that of Moreton waves, these waves seem to be fast-mode MHD waves or shocks (e.g., Chen & Wu 2011; Asai et al. 2012). Recently, some authors linked the EUV waves with direct manifestations of CMEs rather than solar flares, but the exact physical mechanism by which they are related remains unclear (Biesecker et al. 2002; Gallagher & Long 2011; Nitta et al. 2013).

Associated with flares and coronal waves, filaments and prominences at distances are sometimes activated or excited into oscillation. This so-called "winking" (appearing and/or disappearing) motion of a filament is thought to be triggered by a Moreton wave (Smith & Ramsey 1964). Eto et al. (2002) reported the simultaneous observation of an Hα Moreton wave and a winking filament triggered by its association with a solar flare. Winking filaments are more often observed for flares without Moreton waves, whereas Moreton waves are difficult to observe even for large flares. Winking filaments, therefore, constitute indirect evidence of coronal wave traveling in the corona (Shibata et al. 2011), which are called "invisible" Moreton waves (Smith & Harvey 1971). Okamoto et al. (2004) on the other hand, reported a winking filament triggered by the passage of an EIT wave. Takahashi et al. (2015) reported a winking activation in detail caused by an EUV coronal wave. Warmuth et al. (2004b) discussed a schematic outline how to activate a winking filament by a Moreton wave and/or EIT wave. Vršnak et al. (2016), furthermore, showed in their numerical simulation that the lateral expansion during an eruption is important for producing a Moreton wave.

In this paper we examine in detail the coronal disturbance features, such as filament eruption, winking filaments, and EUV waves associated with the M1.6 flare that occurred on 2011 February 16. The EUV coronal wave of this flare has already been discussed (Harra et al. 2011; Veronig et al. 2011). In particular, these authors examined the spectroscopic features, based on the sit-and-stare spectral data in EUVs acquired by the EUV Imaging Spectrometer (EIS; Culhane et al. 2007) on board *Hinode* (Kosugi et al. 2007). We use Hα images taken by the Flare Monitoring Telescope (FMT; Kurokawa et al. 1995) that was installed at National University San Luis Gonzaga of Ica, Peru. We examine in particular the three-dimensional velocity field of the erupted filament and the relation between the Hα filament eruption and the EUV coronal wave. We also examine the relation between winking features of Hα filaments and the EUV coronal wave by analyzing observations from *SDO*/AIA and *STEREO-Ahead* (*STEREO-A*)/SECCHI/EUVI. In Section 2 we describe the data used in this study. The analysis and results are presented in Section 3, and the conclusions are summarized in Section 4.

2. Observations and Data

The flare in question occurred in the Active Region NOAA 11158 (S21°, W30°). It started at 14:19 UT and peaked at 14:25 UT on 2011 February 16, and was classified as M1.6 on the *GOES* scale (Figure 1). NOAA 11158 produced the first X-class flare in the solar cycle 24 during the previous day. Figure 1 shows the time evolution of the *GOES* X-ray emission for the February 16 flare.

For the analysis we use Hα data taken by FMT that provide full-disk solar images in the Hα line center (6562.8 Å), Hα −0.8 Å (blue-wing), Hα +0.8 Å (red-wing), continuum, and limb prominence images (Hα line center with occulting disk). The spatial resolution is about 2.0″, and the time cadence is 20 seconds. Such multiwavelength full-disk observations

with high time cadence are suitable for investigating the velocity field of erupting filaments (Morimoto & Kurokawa 2003a,b; Morimoto et al. 2010) and for detecting Moreton waves (Eto et al. 2002). FMT was relocated in March 2010 from Hida Observatory, Kyoto University to National University San Luis Gonzaga of Ica in Peru by the international collaboration of the Continuous H-Alpha Imaging Network (CHAIN) project (UeNo et al. 2007) for coordinated solar observations.

We cannot find any direct signatures of Hα Moreton waves associated with the flare not only in the FMT images (in Hα line center and the $\pm$0.8 Å wings) but also in their running-difference images. However, we found indirect evidence of the coronal wave in the form of winking filaments that are located far from the flare site. Figure 2 shows a full-disk Hα line center image of the flare taken by FMT. We show the flaring region with f_0 and the filaments are denoted f_1 to f_5. The boxes indicate the areas over which we calculate the intensities to identify their winking features activated by the flare and the coronal waves. Associated with the flare, we also observe a filament eruption whose shape in Hα images looks like a "dandelion". This feature is especially prominent in the red- and blue-wing images. Figure 3 also presents FMT images of the flare, filament eruption, and winking filaments in Hα $-$0.8 Å (left), Hα line center (middle), and Hα +0.8 Å (right) passbands.

The flare was observed in EUV passbands by *SDO*/AIA and *STEREO-A*/SECCHI/EUVI. AIA provides high-resolution full-disk images of the transition region and the corona in multiple wavelengths. We used AIA 171, 304, and mainly 193 Å images to investigate the evolution of the flare, the associated erupting filament, and the coronal waves. The temporal resolution of the AIA 193 Å data, which are attributed to a Fe XII line with the formation temperature of 1.25 MK, is 12 seconds, and the pixel size of the image is 0.60″. At the time of the flare, *STEREO-A* was located 86.8° ahead of the Earth. *STEREO-A*/EUVI images at 195 Å, which again are mainly from the Fe XII line,

have a temporal resolution and pixel size of 5 minutes and 1.58″, respectively.

The flare was also captured in soft X-rays by the X-Ray Telescope (XRT; Golub et al. 2007) on board *Hinode*. XRT is sensitive to hot coronal plasma and can detect emissions from plasma with temperatures of the order of 1 to several tens of MK. We used partial images with 2.5″ pixel resolution through the Thin-Be filter. In addition, to calculate potential magnetic field, we used the Potential Field Source Surface (PFSS) extrapolation model[1] (Schrijver & DeRosa 2003) that was applied to synoptic magnetograms taken by the Michelson Doppler Imager (MDI; Scherrer et al. 1995) on board *SOHO*, based on the LMSAL[2] forecaster program.

3. Analysis and Results

3.1. Overview of active region and of flare

Figure 4 presents the temporal evolution of the flare in various wavelengths. Columns from left to right are images in soft X-rays Thin-Be filter, in EUVs at 171 and 304 Å, and in Hα line center; and were taken by XRT, AIA, and FMT, respectively. Before the flare starts, the so-called "sigmoid" or *S*-shaped magnetic field structure (e.g., Rust & Kumar 1996; Canfield et al. 1999) that lies in the east-west direction is observed in soft X-rays (see top left panel in Figure 4).

During the time of the flare, NOAA 11158 was composed of several sunspots, as discussed in detail by Toriumi et al. (2013) and Sun et al. (2012). In particular, two neighboring fast flux emergences (P_0 - N_0 and P_1 - N_1 pairs) appeared in line along the

[1]http://www.lmsal.com/~derosa/pfsspack/

[2]Lockheed Martin Solar and Astrophysics Laboratory

east-west direction and formed a quadrupolar distribution (see top panel of the Hα -0.8 Å column in Figure 5). Between the following negative spot N_0 of the western bipole and the preceding positive spot P_1 of the eastern bipole appeared a prominent filamentary structure along the magnetic neutral line on February 13, which developed for about three days. The X-class flare on February 15 occurred along the elongated neutral line between N_0 and P_1. This basic magnetic configuration remained even after the X-class flare and displayed the sigmoid structure seen in the XRT images.

The M-class flare in question, however, occurred at the eastern edge of the main neutral line between N_0 and P_1. When the impulsive phase of the flare just begins ($\sim$14:22 UT), a small bright X-ray feature appears at the eastern-end of the sigmoid structure. The brightening has counterparts in Hα and 304 Å images, which are mainly from footpoints of the flaring loops. As of 14:31 UT, the filament eruption can be distinguished in EUV and Hα images (see bottom panels of Figure 4).

The starting point of the filament eruption is also located at the eastern edge of the neutral line between N_0 and P_1. This filament eruption is clearly discernible both in the Hα and EUV images, as shown in Figure 5. It was activated near 14:25 UT and displays an enlarging dark feature in Hα blue-wing images, like a dandelion, whereas no manifestation is exhibited in the Hα red wing until 14:32 UT.

3.2. Eruption of Dandelion filament

Here, we describe how we used Hα images to derive the three-dimensional velocity field of the erupting filament. For the line-of-sight (LOS) velocity, we modified the method by Morimoto & Kurokawa (2003a). They computed the LOS velocities of erupting filaments observed with FMT by using the method based on the Beckers' cloud model (Beckers

1964; Mein & Mein 1988). Morimoto & Kurokawa (2003a) adopted the single cloud model. Because FMT has only three (center and ±0.8 Å) wavelength data points for the four unknowns (source function, optical depth, Doppler velocity, and Doppler width) of a cloud, they further assumed a fixed Doppler width in their calculation. Our method, on the other hand, deals even with the Doppler width as a free parameter. This can be implemented as follows: in the quiescent phase of the filament, we derived the parameters assuming the value of the Doppler width, as was done in Morimoto & Kurokawa (2003a). To analyze a time series, we search for the best-fit solution around the quiescent parameter values found in the initial time step, and select the "nearest" local minimum in the parameter field. This selection of the nearest values is based on the assumption that the physical parameters in a single cloud do not change so quickly. Next, we search the parameters in the next time step around the parameters derived in the previous time step, and so on. We did not set a "pre-defined range" in our method, we used the hybrid method for the fitting (Powell, 1970). The error of the derived LOS velocity is roughly comparable with the errors obtained with the method of Morimoto & Kurokawa (2003a) and is about ± 10 km s^{-1}, while the derived LOS velocity tends to be overestimated for the fixed Doppler width, since the Doppler width is thought to be larger for an erupting filament. The error could be, however, a little bit worse due to misalignment of the wavelengths of the FMT filters from the nominal values. Comparing the wing data, the wavelength of the red wing (+0.8 Å) seems to be set closer to the line center than that of the blue wing (−0.8 Å). The error of the LOS velocity, therefore, is roughly ± 15 km s^{-1}.

The left column in Figure 6 shows the derived temporal evolution maps of the LOS velocity. The colors show blueshift (i.e., moving toward us) and redshift (i.e., moving away from us) of the filament. Near 14:30 UT, the filament begins to erupt northward and simultaneously shows blueshift features, especially at the leading part, with a LOS velocity of about -30 km s^{-1}. At the root of the filament, in contrast, it shows a redshift

with a velocity of about 20 km s^{-1}. The filament eruption is clearly seen until 14:35 UT. At this time, the LOS velocity at the leading edge is nearly −25 km s^{-1}. Next, the front edge gradually becomes invisible at 14:45 UT, whereas near 14:55 UT, the filament shows a dominant redshift pattern. The observed blueshift velocity of about −30 km s^{-1} is slightly larger than the result by Veronig et al. (2011), while the temporal evolution is roughly consistent.

We confirm the temporal LOS motion with the side views of the filament eruption observed from *STEREO-A*, since it was located at 86.8° ahead of the Earth. In the EUV 195 Å images of *STEREO-A*/SECCHI/EUVI, we see movement of the cold plasma as dark features (second column in Figure 5). The dark feature is ejected from the flare site, and the traveling velocity of the front (i.e., the fastest) part is about 280 km s^{-1}. The horizontal component of the velocity (i.e., the velocity in the direction from the Sun to the Earth) is about 230 km s^{-1}. FMT cannot detect clouds with velocity greater than 50 km s^{-1}, because the wavelengths of the wing data are set at ±0.8 Å. Therefore, FMT missed the front part of the ejection.

By comparing the EUVI 195 Å and FMT Hα −0.8 Å images (Figure 5), the Hα filament seems to correspond to the main (i.e., the darkest) part of the filament in the 195 Å images. The main part of the filament has a velocity of about 110 km s^{-1}, and the horizontal component has a velocity of about 90 km s^{-1}. The velocity is much larger than the LOS velocity derived by FMT (30 km s^{-1}). LOS velocities derived from the cloud model reflect representative values of moving clouds, and the fine LOS velocity field in the clouds could be lost. Besides, the velocity in the Earth-Sun direction is derived by following dark features seen in EUVI images, and is not derived by tracing the moving ejecta. Alternatively, we could detect a slower component of the erupting filament, because the velocity of about 90 km s^{-1} far exceeds the detection limit of FMT.

For the tangential velocity of the erupting filament (that is, the velocity of the filament in the plane of the sky), we traced the apparent motion of filament blobs by using the local correlation tracking (LCT) method. The middle column in Figure 6 shows the temporal evolution of the erupting filament with arrows that show the orientation and magnitude of the tangential velocity. The filament blobs are moving upward (i.e., northward) with a tangential velocity of about 10 km s^{-1}. The dark feature seen in EUVI 195 Å images has a northward velocity of about 65 km s^{-1}, which is faster than the tangential velocity derived from FMT. This result is explained by the excessively large mesh size used for the LCT method, which means that features moving at such high speed could not be detected even if they were present. The seeing condition prevents us from reducing the mesh size for the FMT images. Therefore, the derived tangential velocity is a somewhat averaged value of the main part of the ejected filament.

In the right column of Figure 6, we show the temporal evolution of the inclination of the ejecta. The inclination angle is set to zero for the upward direction normal to the solar surface. In the early phase of the ejection (around 14:30 UT), the direction is nearly horizontal with respect to the solar surface, with a slight upward inclination. During the main phase of the ejection, which occurs around 14:35 UT, the direction is still nearly horizontal but with a slight downward inclination. Next, the inclination distribution becomes complex showing upward and downward motions, probably because of the coexistence of upward and downward moving features in the later phase. Although the error in the velocity measurements is probably large, we believe that the ejecta move nearly horizontally with respect to the solar surface. Further, in Figure 5 (EUVI panel at 14:30 UT), we depict the plane of the solar surface (yellow arrows over the heliographic coordinates) and a vertical component perpendicular to the surface (arrow labeled "vertical"). The dashed green arrow highlights the direction of the filament eruption as seen by *STEREO-A*, and φ is the inclination angle with respect to the vertical on the solar

surface. From EUV observations (193 Å and 195 Å) we infer the geometrical components of the erupting material, which led us to estimate $\varphi \approx 58°$. So that, the filament in EUVI was ejected having an elevation angle of about 32°.

3.3. Filament oscillations and EUV waves

In the Hα data, we also observe winking (activation and/or oscillation) of the filaments associated with the flare. As we see in Figure 2, some filaments are labeled f_1 to f_5. These filaments are located far from the flare site. We identify a clear winking feature for filament f_2 and a much fainter signature for filament f_5 (see also the Figure 3).

The time series of the winking filament f_2 is displayed in Figure 7(a) at Hα −0.8 Å (left), Hα center (middle), and Hα +0.8 Å (right) wavelengths. The field of view of the f_2 region is the same as in Figure 2. At 14:40 UT, the filament starts winking. First, a dark feature becomes prominent in the red-wing images, as shown by the arrow labeled $2r$ in Figure 7(a). The feature is dominant until 15:05 UT, and then it fades slowly away. However, at about 14:50 UT, a dark structure starts to appear in the blue-wing images, as pointed out by another arrow ($2b$). This structure is noticeable until 15:10 UT, when it disappears. In the Hα center, in contrast, no significant changes are observed.

Figure 7(c) plots the temporal variations of the intensities calculated for the f_2 region in the three wavelengths. In the red-wing plot (dash-dotted line), we clearly identify a decrease of the intensity associated with the appearance of the dark feature in the red-wing images. The decrease starts at about 14:36 UT and reaches maximal depletion around 14:45 UT, after which it recovers. The signal in the blue-wing plot (dotted line), however, remains roughly constant until 14:55 UT and then starts to decrease gradually. In the Hα center plot (solid line), the signal slightly increases.

A similar analysis for filament f_5 is presented in Figures 7(b) and (d). Unlike f_2, the dark structure appears mainly in the blue-wing (left panels). The dark feature is evident from 14:40 UT until 15:05 UT. Conversely, at 15:00 UT, we recognize a very weak feature in the red-wing (see arrow labeled $5r$ in Figure 7(b)). The temporal variation of the intensities is plotted in Figure 7(d). The winking feature dominates during the darkening of the blue-wing plot (dotted line), whereas the red-wing (dash-dotted line) and Hα center (solid line) plots show gradual variation and no clear signals caused by filament oscillation. For the other filaments f_1, f_3, and f_4, we verified the intensity profiles and found no winking patterns.

We also examine the temporal evolution of the coronal waves associated with the 2011 February 16 flare and the relation with the oscillating filaments. The time sequences of the EUV waves produced by the flare are presented in the top panels of Figure 8 (panels a – d). These are the AIA 193 Å running difference (20-minutes difference) images. The white arrows highlight the moving wavefronts, whereas the locations of the oscillating filaments f_2 and f_5 are marked by the boxes. The distances of the filaments (f_2 and f_5) measured from the flare site along the spherical solar surface are $\approx 5.1 \times 10^5$ and $\approx 6.4 \times 10^5$ km, respectively. We derive the speeds of the EUV wave by following the leading edge of wavefront consecutively along the spherical lines to the filaments f_2 (path 2) and f_5 (path 1) directions. The mean velocities computed from a linear fit are 430 ± 29 km s^{-1} and 672 ± 24 km s^{-1}, respectively. The EUV wave have been studied by several authors (Harra et al. 2011; Veronig et al. 2011; Long et al. 2013; Nitta et al. 2013), and the propagating speed ranges from 500 to 700 km s^{-1}, which changes depending on the propagating direction. Therefore, the velocities derived in this study are comparable with those results.

At 14:28 UT (Figure 8a), a well-defined wavefront propagates mainly toward the north,

and a bright erupting material is observed that corresponds to the dandelion filament. At about 14:31 UT (Figure 8b), the central part of the wavefront seems to stop and to exhibit a stronger amplitude: this occurs just when the wave is approaching the edges of a weak active region that is located north of NOAA 11158. The observed enhanced pattern and the changes in the wavefront progression are tentatively attributed to the compression of plasma generated by the interaction between the coronal wave and the confined magnetic system of the active region (Uchida 1974). We plot the potential magnetic field configuration derived by *SOHO*/MDI in Figure 8(e). The red triangle indicates the location of the northern weak active region. We confirm that the propagating wavefront tends to stop there. Note that, at 14:35 UT (Figure 8c), the leading part of the wavefront decelerates, perhaps retained by the magnetic field configuration, whereas the west part is slightly refracted and continues traveling northwest (Figure 8d).

Figure 8(f) shows the progression of the most prominent fronts of the EUV wave from 14:27 to 14:40 UT, the positions of the weak active region, and the oscillating filaments f_2 and f_5. At 14:37 UT, the wavefront labeled 5 approaches f_5 and, at 14:40 UT, wavefront 6 reaches f_2. These times are consistent with those identified both in the images and in the intensity plots of f_2 and f_5 (Figure 7). Figure 9 presents the time-distance diagram of these temporal behaviors. We measured the temporal evolution of the wavefronts along the paths, as shown by the projected dashed lines in Figure 8(f). The squares $\Box$ and circles $\circ$ plotted together with linear fit (dotted lines) in Figure 9 show the times and the positions of the wavefronts as they move along paths 1 and 2, respectively. Diamonds $\diamond$ indicate the oscillating filaments f_5 and f_2, which are on straight lines, as shown by the dotted lines. Therefore, the observed winking filaments are assumed to have been triggered by the passage of the EUV coronal wave.

4. Summary and Conclusions

We observed a filament eruption shaped like a dandelion and associated with the flare that occurred at NOAA 11158. We analyze the Hα images taken with FMT in Peru and derive the three-dimensional velocity field by using a new method. To derive the LOS velocity, we use the modified cloud model that was originally developed for the FMT data by Morimoto & Kurokawa (2003a). We compare the temporal behavior of the erupting dandelion filament with its EUV side views observed by *STEREO-A*/SECCHI/EUVI. We realize that the LOS velocity derived from Hα images of FMT gives representative values of the moving clouds and that the very fast components seen in the *STEREO-A*/EUVI images are probably lost due to the detection limit of FMT. The tangential velocity of the dandelion filament is derived by applying the local correlation tracking (LCT) method to the Hα images. We derive a representative (averaged) tangential velocity of the main part of the filament, although we could not capture small fast-moving features, if they exist, because of the limited mesh size of the LCT method. By combining these LOS and tangential velocities, and applying a coordinate transformation, we also derive the inclination of its velocity vectors. We confirm that the dandelion filament is ejected nearly horizontally with respect to the solar surface.

We also observe the winking of Hα filaments that are located far from the flare site, and examine the relation between the winking filaments and the EUV coronal wave associated with the flare. As summarized in Figures 8 and 9, Hα filaments f_2 and f_5 start oscillating when the EUV coronal wave arrives, so we confirm that the interaction between the EUV wave and the Hα filaments causes the filaments to wink.

The derived traveling speed of the observed EUV waves is about 430 to 672 km s^{-1}. Associated with this flare, Type II radio burst was also observed (Harra et al. 2011; Nitta et al. 2013). These results are a strong indication that the observed EUV waves

are MHD fast-mode wave or shock. Moreover, we observed the filament eruption ejected tangentially to the solar surface. This seems to be suitable to generate a Hα Moreton wave, because the wavefront could easily make contact with the chromospheric plasma, even if a shock front is generated only in some restricted range at the front of the ejected filament. Nevertheless, we do not observe the Moreton wave associated with the flare. This is probably because the downward velocity of the wavefront is small (about 20 km s^{-1}) toward the solar surface, as reported by Harra et al. (2011) and Veronig et al. (2011), and probably because the EUV coronal wave (or shock) is not strong enough to generate an observable Moreton wave in the Hα band.

We derived the three-dimensional velocity field of the filament eruption. We could follow the temporal evolutions of the velocity field and inclination of the ejecta. We also examined the temporal behaviors of the EUV waves associated with the filament eruption. These provide us an overall picture on the development of the EUV coronal wave and a filament ejection. Although FMT may have missed to capture very fast components the close correlations in time and main direction of the EUV wave progression with those of the filament eruption, leads us to conclude that the filament is the driver of the observed EUV wave. Although the work we did by measuring the three-dimensional velocity fields of erupting filament and examining the relation between velocity fields and coronal EUV wave have shown a direct link among both phenomena, further studies are needed to fully understand filament eruptions as a driver of coronal EUV waves and coronal mass ejections (CMEs). Statistical studies to derive the tendency of filament eruptions to generate coronal waves and/or CMEs could be useful for this.

We are grateful to the anonymous referee for helping us to clarify and improve this manuscript. DPC expresses special thanks to Dr. Mutsumi Ishitsuka for motivation and an invitation into the world of solar physics research, and is very grateful to all the

staff members of the Kwasan and Hida observatories of Japan for all of the support and discussions during the FMT workshops and working-group meetings conducted in Japan and in Peru. The authors are also grateful to the SDO/AIA and STEREO/EUVI teams for providing the high quality data used in this study. *Hinode* is a Japanese mission developed, launched, and operated by ISAS/JAXA, in partnership with NAOJ, NASA and STFC (UK). Additional operational support is provided by ESA and NSC (Norway). This work was supported by JSPS KAKENHI Grant Numbers 25287039 and 15K17772, and also by the international program "Climate And Weather of the Sun-Earth System - II (CAWSES-II): Towards Solar Maximum" sponsored by SCOSTEP. This work was also supported by the "UCHUGAKU" project of the Unit of Synergetic Studies for Space, Kyoto University. AA is supported by Shiseido Female Researcher Science Grant.

Facilities: FMT, SDO (AIA), Hinode, STEREO (SECCHI/EUVI), SOHO (MDI)

REFERENCES

Asai, A., Ishii, T. T., Isobe, H., et al., 2012, ApJ, 745, L18

Athay, R. G., Moreton, G. E., 1961, ApJ, 133, 935-945

Beckers, J. M., 1964, PhD Thesis, University of Utrecht

Biesecker, D.A., Thompson, B.J., Hammer, D.M., Vourlidas, A., 2002, ApJ, 569, 1009-1015

Canfield, R. C., Hudson, H. S., Mackenzie, D. E., 1999, Geophys. Res. Lett., 26, 627-630

Chen, P. F., Wu, Y., 2011, ApJ, 732, L20

Culhane, L., Harra, L. K., Baker, D., et al., 2007, PASJ, 59, S751-S756

Delaboudinière, J.-P., Artzner, G. E., et al., 1995, Sol. Phys., 162, 291-312

Domingo, V., Fleck, B., Poland, A. I., 1995, Sol. Phys., 162, 1-37

Eto, S., Isobe, H., Narukage, N., et al., 2002, PASJ, 54, 481-491

Gallagher, P.T., & Long, D.M., 2011, Space Sci. Rev., 158:365-396

Golub, L., Deluca, E., Austin, G., et al., 2007, Sol. Phys., 243, 63-86

Harra, L. K., Sterling, A. C., Gömöry, P., Veronig, A., 2011, ApJ, 737, L4

Howard, R. A., Moses, J. D., Vourlidas, A., et al., 2008, Space Sci. Rev., 136, 67-115

Kai, K. 1970, Sol. Phys., 11, 310

Kaiser, M. L., Kucera, T. A., Davila, J. M., St. Cyr, O. C., Guhathakurta, M., Christian, E., 2008, Space Sci. Rev., 136, 5-16

Klassen A., Aurass, H., Mann, G., Thompson, B.J., 2000, A&AS, 141, 357-369

Kosugi, T., Matsuzaki, K., Sakao, T., et al., 2007, Sol. Phys., 243, 3-17

Kurokawa, H., Ishiura, K., Kimura, G., Nakai, Y., Kitai, R., Funakoshi, Y., Shinkawa, T., 1995, J. Geomag. Geoelectr., 47, 1043-1052

Lemen, J. R., Title, A., Akin, D. J., et al., 2012, Sol. Phys., 275, 17-40

Long, D. M., Williams, D. R., Régnier, S., Harra, L. K., 2013, Sol. Phys., 288, 567-583

Mein, P., Mein, N., 1988, A&A, 203, 162-169

Moreton, G. E., 1960, AJ, 65, 494

Moreton, G. E., Ramsey, H. E., 1960, PASP, 72, 357-358

Morimoto, T. & Kurokawa, H., 2003a, PASJ, 55, 503-518

Morimoto, T. & Kurokawa, H., 2003b, PASJ, 55, 1141-1151

Morimoto, T., Kurokawa, H., Shibata, K., Ishii, T. T., 2010, PASJ, 62, 939-949

Nitta, N.V., Schrijver, C.J., Title, A.M., Lui W., 2013, ApJ, 776, 58(13pp)

Okamoto, T. J., Nakai, H., Keiyama, A., Narukage, N., UeNo, S., Kitai, R., Kurokawa, H., Shibata, K., 2004, ApJ, 608, 1124-1132

Patsourakos, S., Vourlidas, A., 2012, Sol. Phys., 281, 187-222

Pesnell, W. D., Thompson, B. J., Chamberlin, P. C., 2012, Sol. Phys., 275, 3-15

Powell, M.J.D., 1970, A Hybrid Method for Non-Linear Equations, Ed.: Gordon & Breach

Rust, D. M., Kumar, A., 1996, ApJ, 464, L199-L202

Scherrer, P. H., Bogart, R. S., Bush, R. I., et al., 1995, Sol. Phys., 162, 129-188

Schrijver, C. J., DeRosa, M. L., 2003, Sol. Phys., 212, 165-200

Shibata, K., Kitai, R., Katoda, M., et al., 2011, Solar Activity in 1992-2003, (Kyoto: Kyoto University Press)

Smith, S. F. & Harvey, K. L., 1971, in Physics of the Solar Corona, ed. C. J. Macris (Dordrecht: Reidel), 156

Smith, S. F. & Ramsey, H. E., Z. Astrophys., 1964, 60, 1

Sun, X., Hoeksema, T., Liu Y., Wiegelmann T., Hayashi, K., Chen, Q., Thalmann, J., 2012, ApJ, 787, 77

Takahashi, T., Asai, A., Shibata, K., 2015, ApJ,801, 37

Thompson, B. J., Gurman, J. B., Neupert, W. M., et al., 1999, ApJ, 517, L151-L154

Thompson & Myers., 2009, ApJS, 183, 225

Thompson, B.J., 2000, Sol. Phys., 193, 161

Toriumi, S., Iida, Y., Bamba, Y., Kusano, K., Imada, S., Inoue, S., 2013, ApJ, 773, 128

Uchida, Y., 1968, Sol. Phys., 4, 30-44

Uchida, Y., 1974, Sol. Phys., 39, 431-449

UeNo, S., Shibata, K., Kimura, G., Nakatani, Y., Kitai, R., Nagata, S., 2007, Bull. Astr. Soc. India, 35, 697-704

Veronig, A. M., Gömöry P., Kienreich, I. W., Muhr, N., Vršnak, B., Temmer, M., Warren P. H., 2011, ApJ, 743, L10

Vršnak, B., Žic T., Lulić S., Temmer M., Veronig A.M., 2016, Sol. Phys., 219,89-115

Warmuth, A., Vršnak, B., Magdalenić, J., Hanslmeier A., Otruba, W., 2004a, A&A, 418, 1101-1115

Warmuth, A., Vršnak, B., Magdalenić, J., Hanslmeier A., Otruba, W., 2004b, A&A, 418, 1117-1129

Warmuth, A., 2015, LRSP, 12, 3

This manuscript was prepared with the AAS LaTeX macros v5.2.

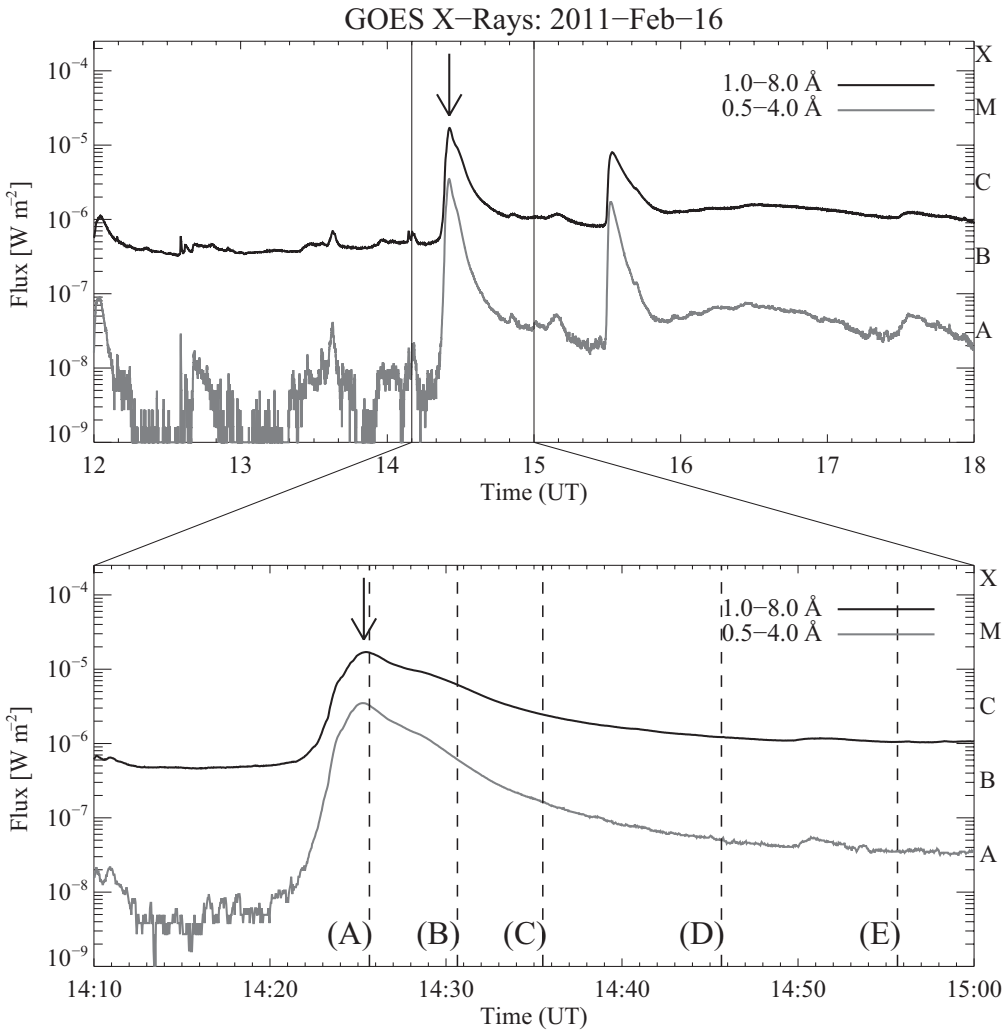

Fig. 1.— *GOES* X-ray emission at 1.0-8.0 Å and 0.5-4.0 Å channels of the 2011 February 16 flare (with extended time range at the top and an enlarged view in the bottom panels). The arrows indicate the peak of the M1.6 flare at 14:25:20 UT, which occurred in the Active Region NOAA 11158. The second peak at 15:32 UT in the top panel corresponds to a C7.7 flare that occurred in the same active region. The vertical dashed lines in the bottom panel point out the times of the images shown in Figures 5 and 6.

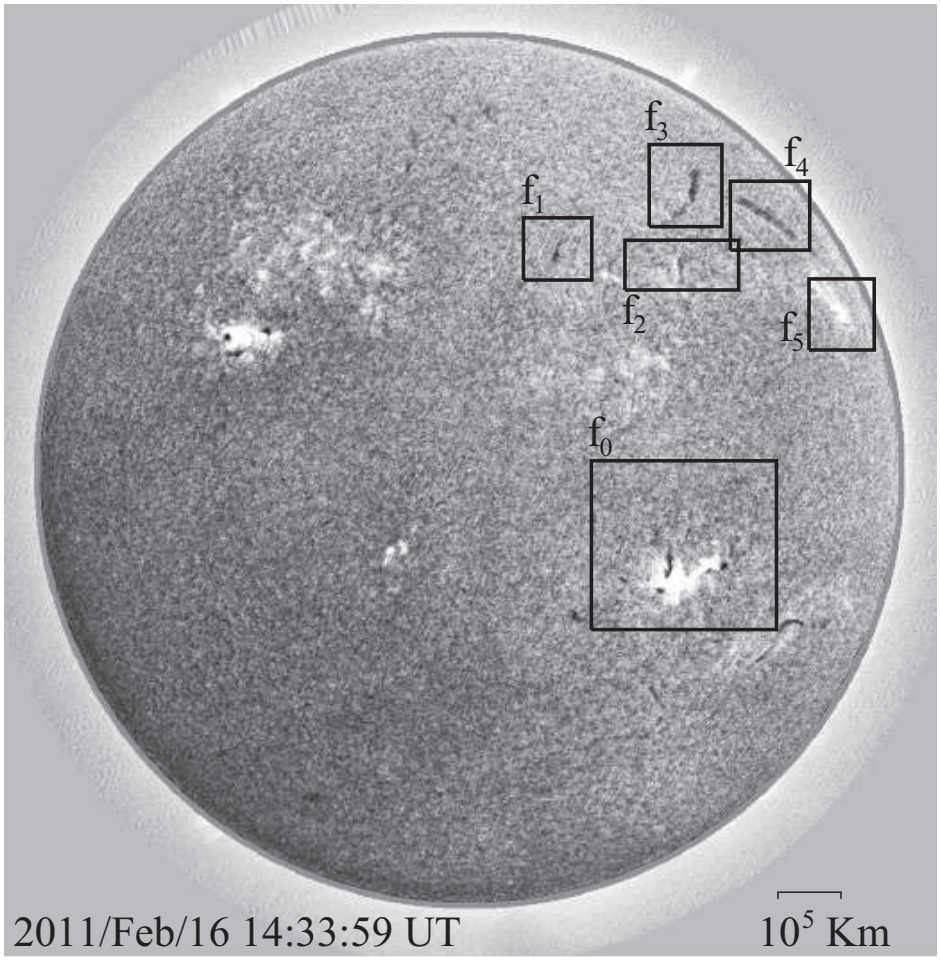

Fig. 2.— Full disk solar image (solar north is up and west is to the right) of the flare in Hα line center taken by the FMT at National University San Luis Gonzaga of Ica, Peru. The box f_0 shows the flaring region, whereas the fields of view f_1 to f_5 contain the quiescent filaments. Filaments f_2 and f_5 are analyzed in more detail in Figure 7.

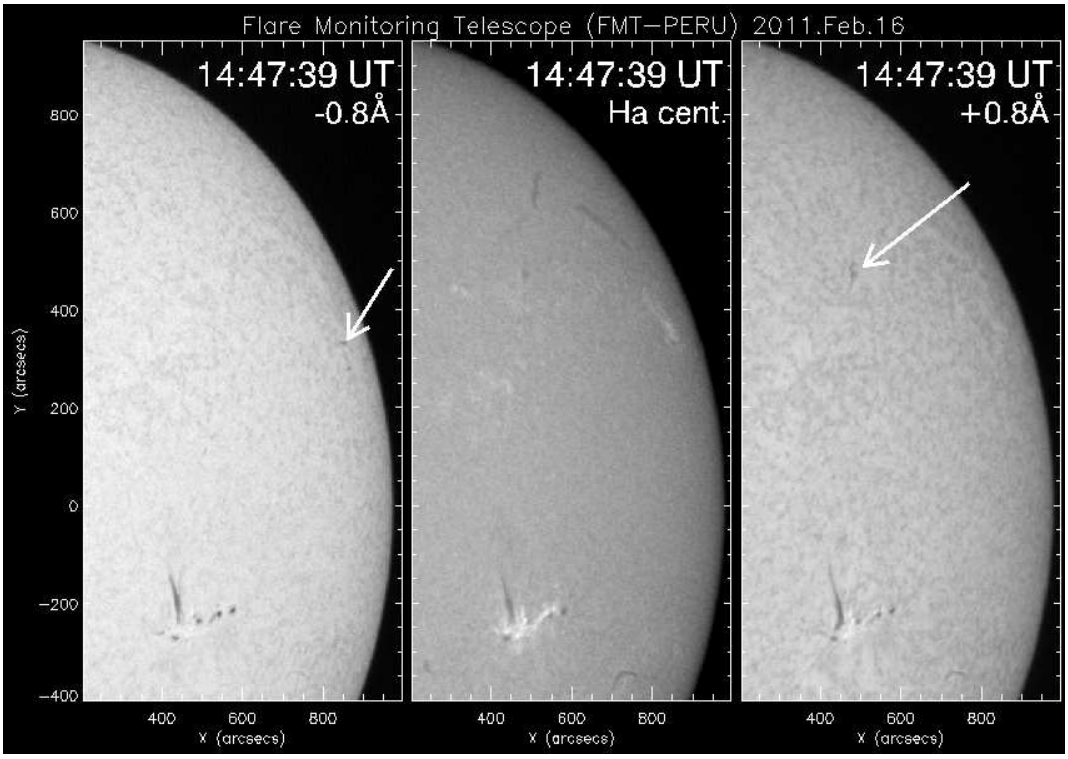

Fig. 3.— Temporal evolution of the filament eruption and the oscillating filaments (arrows), associated with the 2011 February 16 flare. Hα -0.8Å (left panel), Hα line center (middle panel), and Hα $+0.8$Å (right panel) images taken by FMT are shown. [See the electric edition of the Journal for an associated animation].

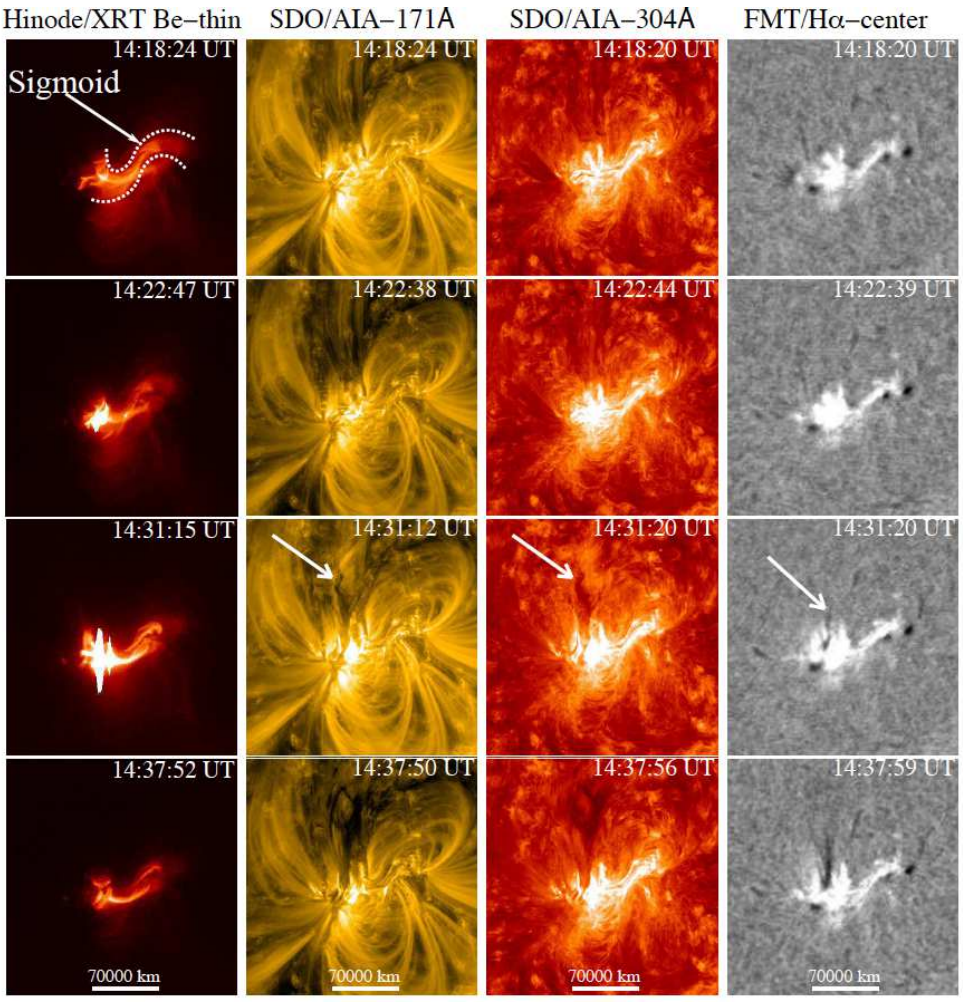

Fig. 4.— Multiwavelength time sequences of the 2011 February 16 flare. Columns from left to right are *Hinode* XRT Thin-Be broadband filter, *SDO*/AIA at 171 and 304 Å, and FMT Hα line center images. At 14:18 UT a sigmoid structure is clearly observed in X-ray images, the dotted lines outline the sigmoidal shape prior to the flare. In 171 Å, 304 Å, and Hα images a dark feature (filament eruption) becomes visible as of 14:31 UT. We pointed out the dark features by arrows.

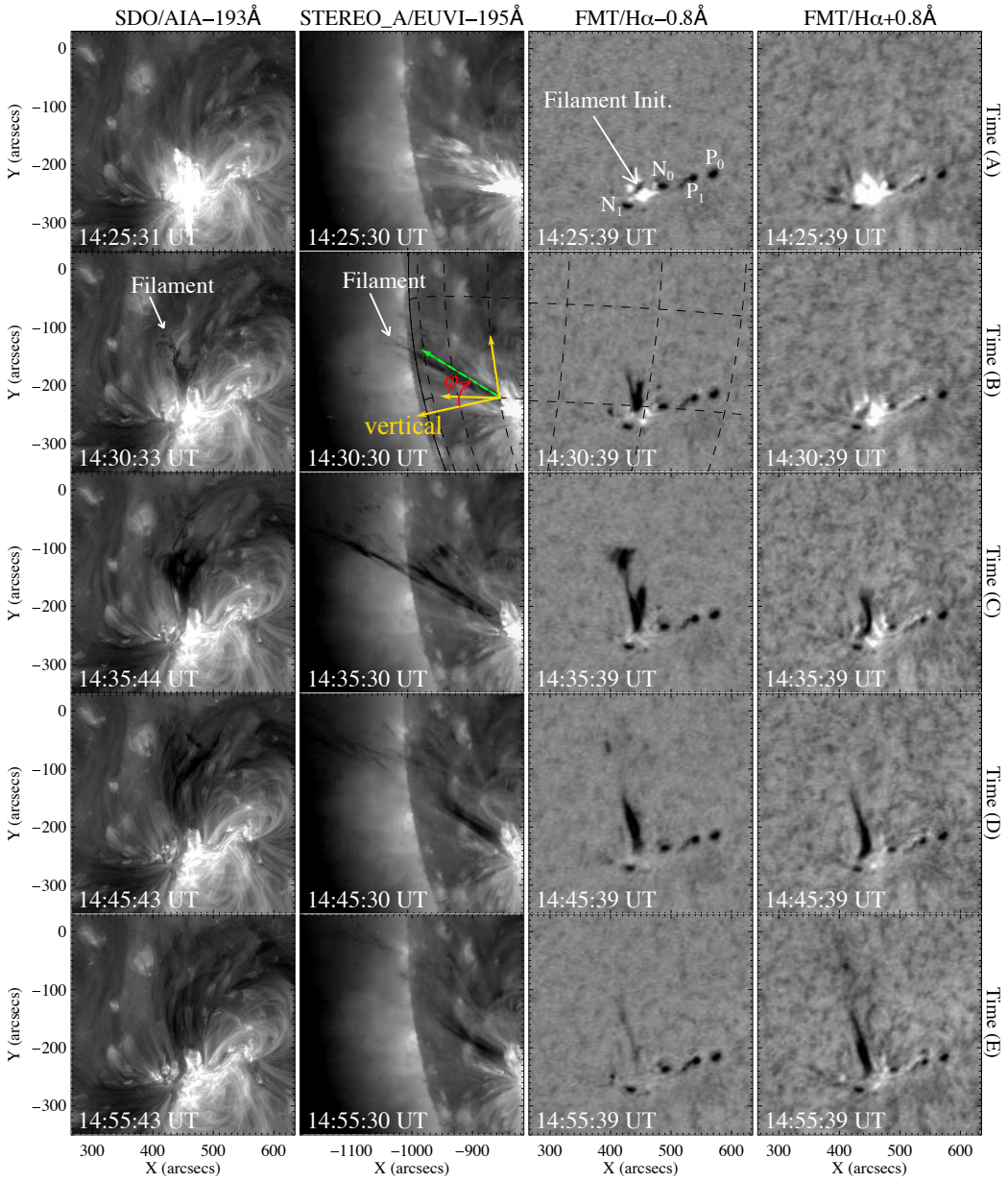

Fig. 5.— Temporal evolution of filament eruption. From left to right: AIA 193 Å, EUVI 195 Å, and FMT Hα −0.8 and +0.8 Å images. The *STEREO-A*/SECCHI/EUVI images show the side view of the filament, since it was located 86.8° ahead of the Earth. The dashed green arrow at 14:30 UT point out the direction of the ejecta and the yellow arrows constitute the projected plane on the solar surface, φ is the inclination angle with respect to the vertical component normal from the solar surface. In the top panel of the third column, the arrow indicates the location of the erupting filament, whereas P_0, N_0, P_1, and N_1 denote the sunspot distributions.

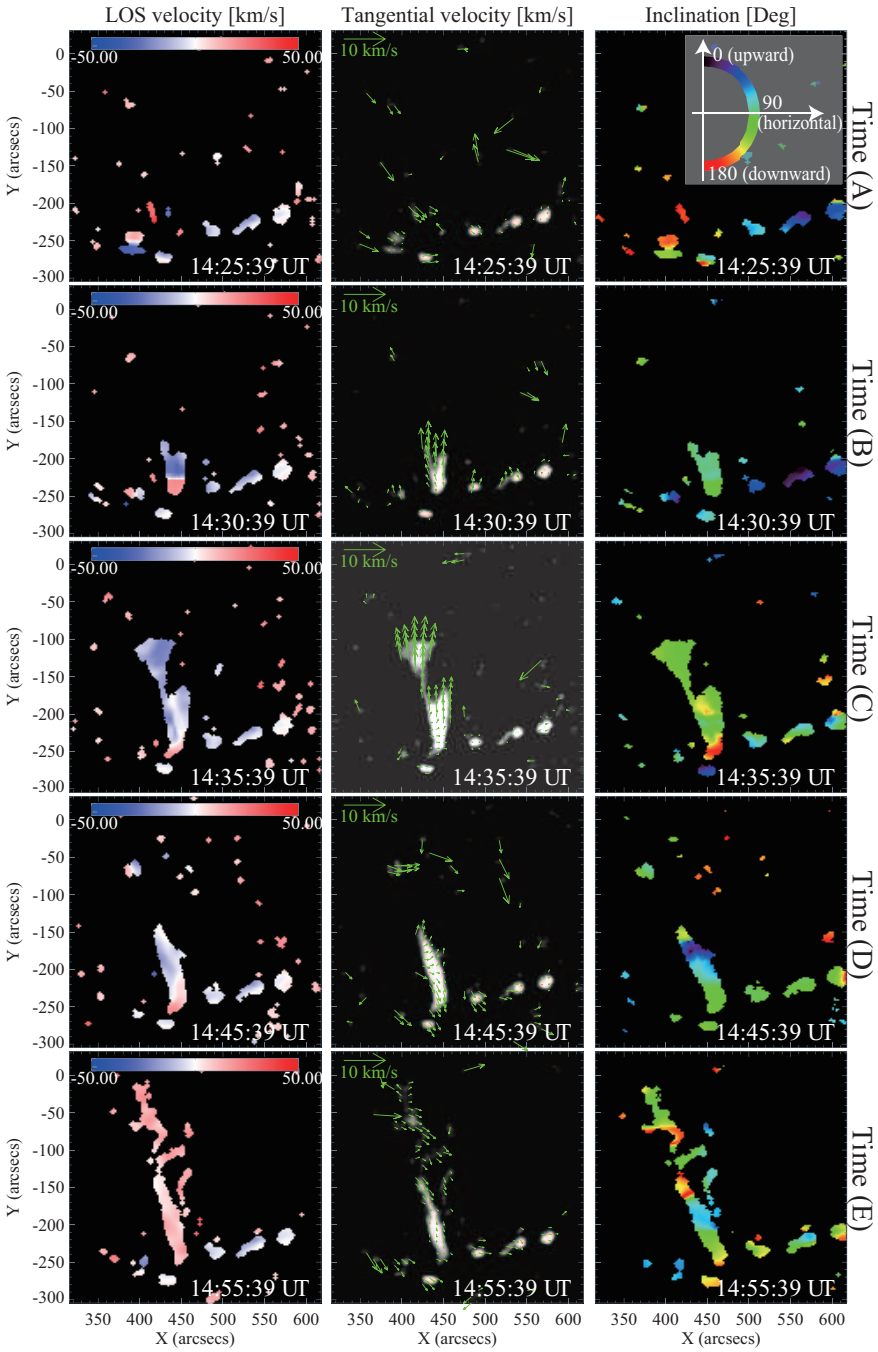

Fig. 6.— Line-of-sight (LOS) velocity (left column), tangential velocity (middle column), and inclination (left column) maps of the erupting filament. The LOS velocity was obtained by calculating the Hα profile based on the cloud model. The tangential velocity was calculated by tracing the motion of the internal structures in successive images. The inclination is the result of the coordinate transformation of the velocity vectors and corresponds the top view of the filament, which is normal to the solar surface.

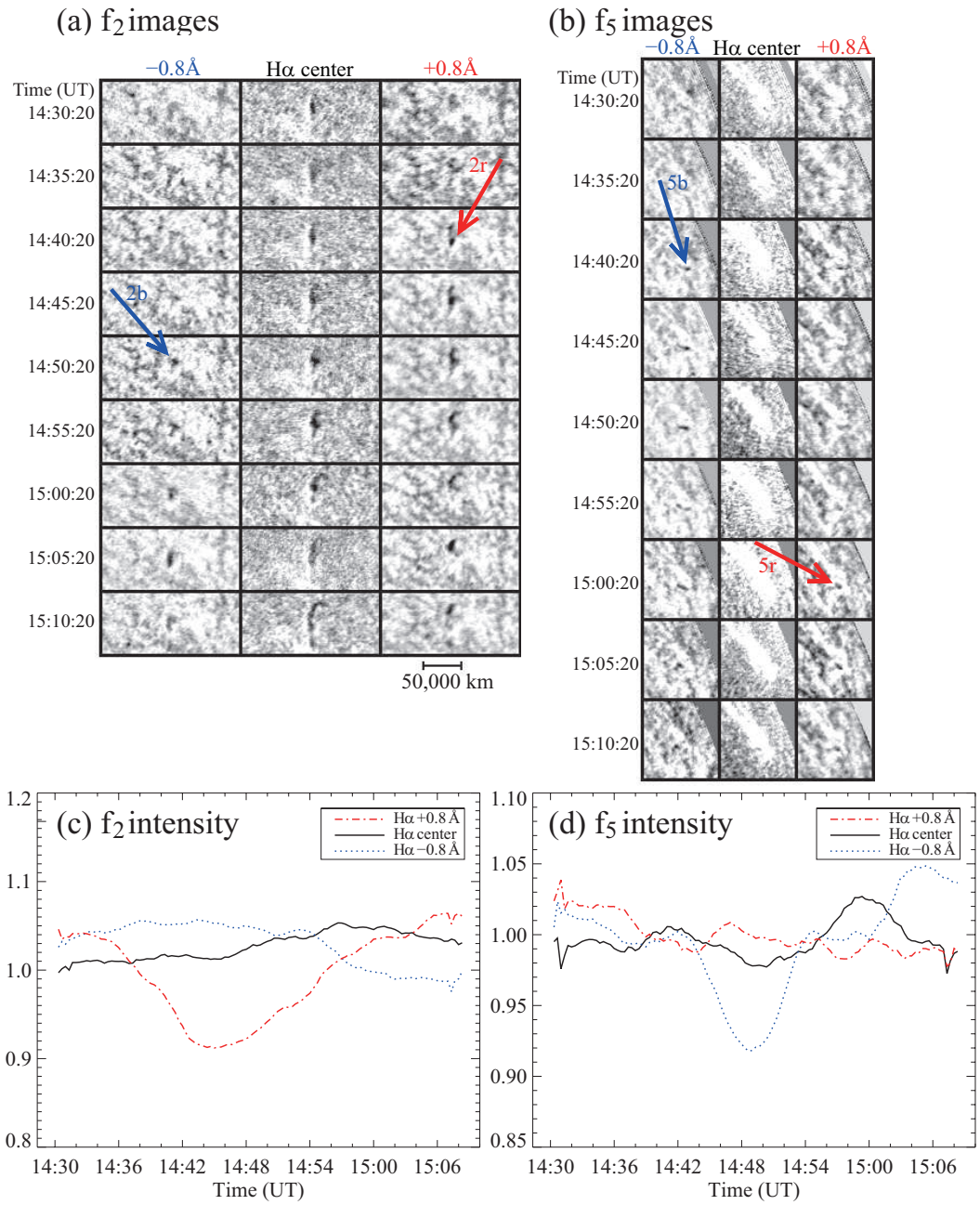

Fig. 7.— (a), (b) Hα images: Hα −0.8 Å (left), Hα center (middle), and Hα +0.8 Å (right) of the oscillating filaments f_2 and f_5, respectively. The field of view is shown in Figure 2. The arrows indicate the starting time of the oscillation both in Hα +0.8 Å (labeled 2r and 5r) and Hα −0.8 Å (2b and 5b). (c), (d) Time profiles of intensities for regions f_2 and f_5, respectively. The horizontal axis is the time in UT, and the vertical axis is the normalized intensity. The solid, dotted, and dash-dot lines are the intensities in Hα center, −0.8 Å, and +0.8 Å, respectively.

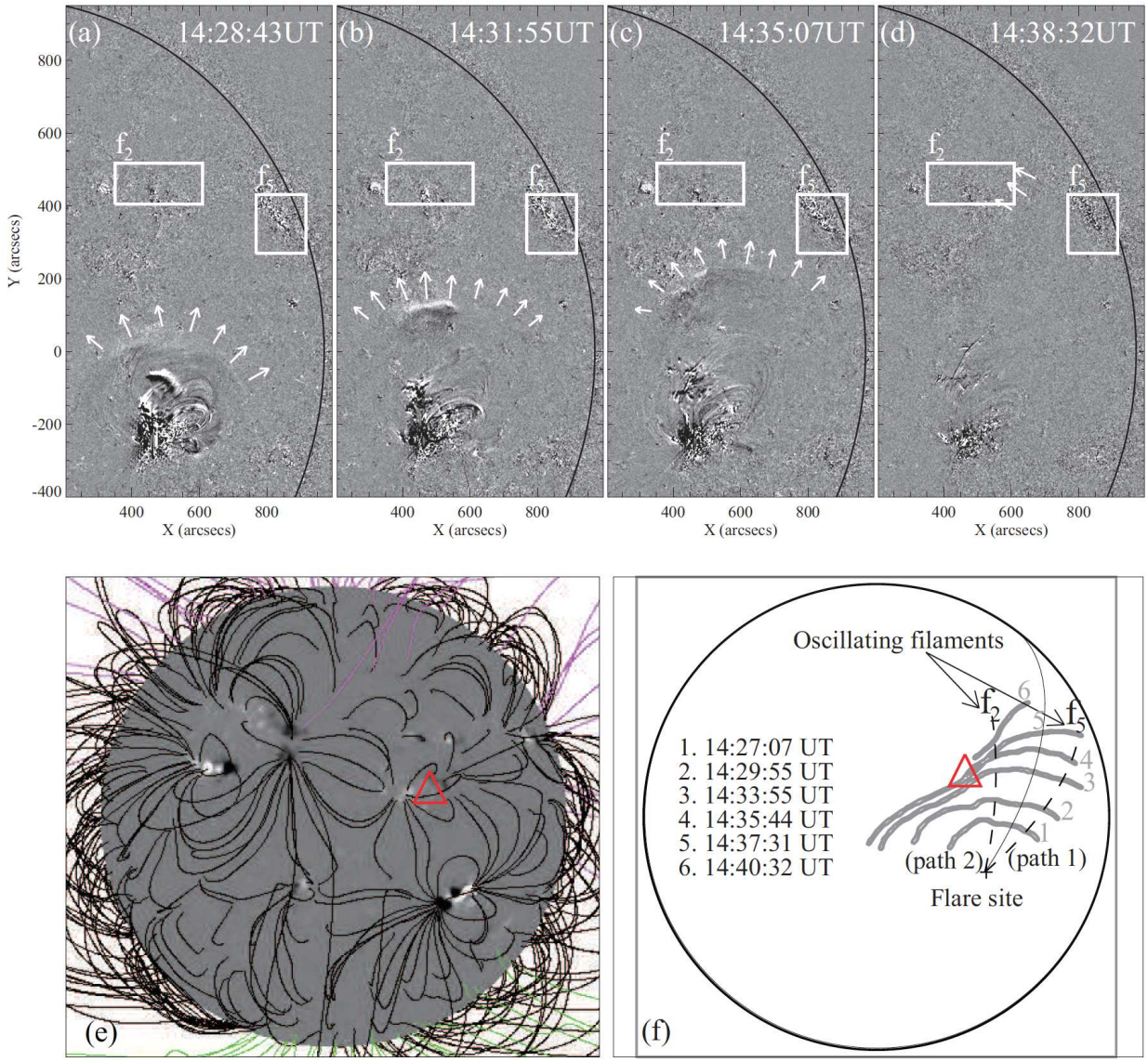

Fig. 8.— (a) – (d) Time sequences of running difference images of the *SDO*/AIA 193 Å images. The regions of the Hα filaments f_2 and f_5 are marked by the rectangles. (e) Potential magnetic field configuration extrapolated from the *SOHO*/MDI magnetogram based on the PFSS model. The red triangle denotes the location of the weak active region. (f): A schematic illustration of the coronal wave progression and its interaction with the filaments f_2 and f_5. The gray strokes outline the wavefronts at the given time and the arrows indicate the filaments position.

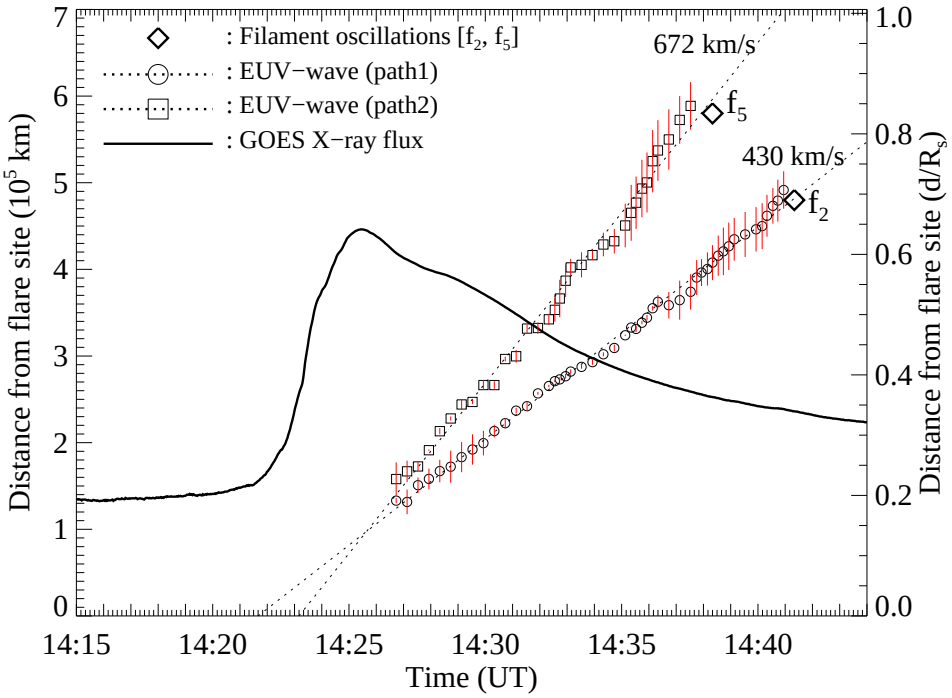

Fig. 9.— Time-distance diagram of EUV wave and oscillating filaments f_2 and f_5, measured along the paths shown by dashed lines in Figure 8(f). The diamonds ◇ mark the positions of filaments f_2 and f_5, whereas the wavefront distances at given time are represented by ○ and □ together with the standard deviation (error bars) along paths 1 and 2, respectively. R_s is the solar radius (≈695 800 km). For comparison, we also plot the *GOES* X-ray flux in the 1.0-8.0 Å channel (solid line).